

A new model of organic solar cells reveals open circuit conditions and size dependent power loss induced by the finite conductivity of a transparent contact

Dor Gotleyb^{a)} and Rafi Shikler

Department of Electrical and Computer Engineering, Ben-Gurion University of the Negev, Beer-Sheva 8410501, Israel

(Received 11 August 2016; accepted 10 January 2017; published online 27 January 2017)

We report on a new approach to modelling the effect of the size of organic solar cells on their efficiency. Experimental results show a drastic deterioration in performance when scaling up organic solar cells. This reduction reflects in key parameters such as the short circuit current (I_{sc}), the maximum power point (P_m), and the Fill Factor (FF). It is attributed to the transparent anode that exhibits a relatively low conductivity (σ). Our unique approach is to account for the interplay between the two sub-domains of the solar cell. In the first domain, containing the electro-optic active materials, we solve the drift-diffusion model using a simplified model for the recombination to emphasize the role of the anode resistance. In the second domain, representing the anode, we solve only the Laplace equation. We introduce the coupling between these layers using the current of the active layer as the boundary condition for the anode and the position dependent potential of the anode as the boundary condition for the active layer. Our results reveal that as the length of the cell increases, the parts that are farther from the contact exhibit near open circuit conditions and do not contribute to the current. We found that the efficiency of the cell altered from linear to sub-linear behavior already at cell lengths of a few millimeters. The transition point strongly depends on the conductivity of the anode. The sub-linearity starts at 0.4, 0.5, and 0.7 cm for $\sigma = 100, 200$, and 500 S/cm, respectively. Additionally, the efficiency begins to saturate sooner than both the short circuit current and the Fill-Factor. The saturation is observed at device lengths of 0.8, 1.2, and 2.1 cm for $\sigma = 100, 200$, and 500 S/cm, respectively. *Published by AIP Publishing.* [<http://dx.doi.org/10.1063/1.4974537>]

I. INTRODUCTION

The study of organic solar cells (OSCs) has been rapidly developed in recent years. Vast efforts were invested in pursuing suitable compounds, structures, and processes for optimizing solar cell's performance. Nowadays, the power conversion efficiencies of OSCs are higher than 10%.¹ OSC technology is sought after mainly due to the ease of manufacture using solution-based processing techniques, such as spin coating and inkjet printing,^{2,3} and their exclusive properties, such as mechanical flexibility, light-weight, and transparency. These properties enable OSCs to be used in unconventional applications such as smart windows^{4,5} and utilized on surfaces that are not suited for conventional solar cells. However, in order for OSCs to be applicable for these unconventional applications, their current dimensions of a few millimeters square must be increased by at least an order of magnitude. A discussion of the possible architectures, their differences, and their upscaling potential is presented elsewhere.⁶ Experiments done on scaling up the OSC area^{7–11} show that the increase of the short circuit current (I_{sc}) and of the maximum power point (P_m), as the device size increases, is sublinear and even saturated. This together with the observation that the Fill Factor (FF) is reduced

stands in contrast to the expected linear behavior and implies that the power conversion efficiency will follow a similar behavior.

The observed losses are attributed to the transparent anode¹² that covers the entire electro-optic active layer (EOAL), where light is absorbed and charge separation processes occur. The reason that the entire EOAL surface is covered by the anode is because charge carrier diffusion lengths in organic materials are rather small (≤ 10 nm).^{13,14} It requires the EOAL to be fully covered by the anode for all the charges to be extracted. As such, the anode must be transparent. However, transparency and conductivity properties, in materials relevant for anode use, are contradictory to each other. As transparency grows, conductivity decreases and vice-versa. Experimental results exemplifying this phenomenon are reviewed in the work by Ellmer.¹⁵ Comparison of different experimental data concerning thin graphene films has been performed by De and Coleman, who conducted a figure of merit to account for the relation between transparency and conductivity.¹⁶ Although their work concentrated on a specific kind of anode, it can be easily generalized to account for other potential materials. All these results support the assumption that the transparent contact causes power loss in the device as its dimensions get larger.¹⁷ Extensive experimental research has been conducted in order to improve the large area device's performance,¹⁸ not only electrically but also mechanically.¹⁹ Such research is directed toward

^{a)}Author to whom correspondence should be addressed. Electronic mail: Gotleyb@post.bgu.ac.il

searching new anode materials, such as PEDOT:PSS²⁰ (Poly(3,4-Ethylenedioxythiophene) Polystyrene Sulfonate) and graphene films,²¹ enhancing anode conductivities,²² and understanding their limitations. One promising solution to overcome the low conductivity limitation is to include a metal grid on top of the anode.^{23–26} Clear enough, this metal grid reduces light in the EOAL, and it appreciably complicates the fabrication process. Thus, with the use of proper fabrication techniques^{27,28} and proper simulations, an optimization between transparency and conductivity of the anode and the optimized shape and size of such metal can be achieved.

To complement these experimental works, namely, understanding the observations, and predict the large area device's behavior, a comprehensive model is needed. Usually, the loss (attributed to the anode) is modeled by a somewhat naive equivalent circuit¹⁷ where an additional series resistance is included to account for the anode resistivity. As mentioned by Katz *et al.*,²⁹ this model does not take into account the varying nature of the circuit parameters in organics, e.g., exciton dissociation probability is a function of the voltage distribution within the device. They suggested an improved model in the form of a distributed equivalent circuit that also accounts for the interplay between the anode and the EOAL. Despite the advantages of this model, this is again just a partial description of the actual dynamics in the device since it just replaces a one cell model with a series of cells where the smallest cell size with its characteristics is yet to be determined.

A more appropriate methodology would be to treat EOAL and anode as separate domains, each expressed with different models, and later on to combine them together self consistently. To account for the finite conductivity (σ) of the anode, Galagan *et al.* suggested to solve the Laplace equation [see Eq. (1)] within this resistive medium.^{30,31} A description for the EOAL can be achieved by solving the basic equivalent circuit model,³² as already mentioned, or by approximating the cell's behavior using the experimental data.³⁰ These approaches are oversimplified and self-consistency can only partially be achieved. Next, a matching of the Laplace equation with a description of the EOAL is required. Although the described procedure has been made, the description of the EOAL and the matching of the two domains have performed inadequately. Therefore, the interplay between the EOAL and the contact has been neglected, and such simulations cannot be used to predict results for different materials and geometries. More in-depth models counting the physical processes in the cell are needed. Such models can be in the form of rate equations or continuity equations. Such a rate equation model was utilized by Tessler in order to study a range of physical aspects, for instance, different recombination mechanisms^{33,34} and the influence of different contact barriers.³⁵ Despite it being a fundamental model, it is very complicated, especially in the two dimensional situation, which is needed for accounting for the impact of the anode and then again neglecting the spatial dependence, which is necessary to account for the interplay of the two domains.

The interplay, i.e., the nature of charge injection and extraction at the electrodes, is known to be a major limitation mechanism on the performance of OSCs. It is, therefore, highly important to appropriately define the interaction between the two layers. In practice, there exists a Schottky barrier at the interface, which impairs the extraction of charges. There has been, however, several works that demonstrated the formation of such ohmic contacts or quasi ohmic contacts by surface treatments³⁶ or by introducing buffer layers at the interface.^{37–40} Such experiments lay the foundations for high efficient OSCs. Together with supporting simulations accounting for the nature of the interplay, future designs of OSCs can be improved one step further.

In order to fully understand the effect of anode's size on OSC performance, it is important to develop a model that combines both the electrodes and the EOAL. We report on an innovative 2D simulation based on the fundamental physics of charge transport in organic materials, which also accounts for the losses introduced by the anode. Based on the material parameters and geometries of the device, we were able to study the performances of the large area device and the influence of different anode conductivities. With this model, we hope to get physical insights on the origin of experimental findings such as the Fill-Factor and short circuit current dependence on the OSC properties.⁴¹ Moreover, it will allow investigating the relation between transparency and conductivity in a rigorous way as well as the influence of other parameters, such as light intensity.⁴² It will also allow us to decouple the effect of the anode from the effects of different processes within the EOAL, such as different recombination mechanisms.

II. MODELING OF AN ORGANIC SOLAR CELL

Our approach to OSC modeling aims to give a comprehensive description of the physical processes that take place within all the different sub-domains of the device. The OSC cannot be seen as a detached single unit but should rather be considered as an assemblage of several layers of different materials and different functionalities. The proposed model aims at describing the three most important layers of the device and to create a framework that can be easily extended to account for additional layers.

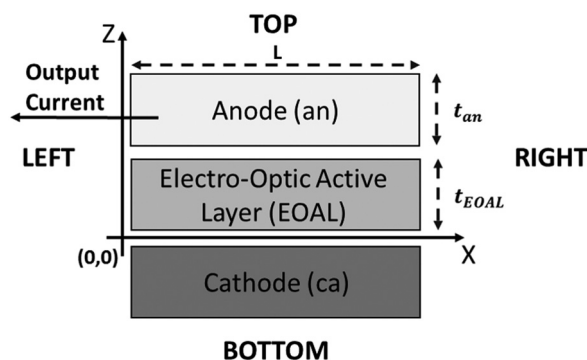


FIG. 1. A cross-section of a basic OSC device: From the direction of the incoming light, anode (front contact), electro-optic active layer, and cathode (back contact).

A typical cross-section of an OSC is shown in Fig. 1. It is composed of the following layers: in the direction of the incoming light, anode (front contact), electro-optic active layer, and cathode (back contact). In the commonly used models, the only functions of the electrodes are to dictate the boundary conditions for the optical flux and for the potential $V_{EOAL}(x, z)$ along the EOAL interfaces. Both are assumed to be position independent.

The EOAL is a blend of donor like and acceptor like organic semiconductors. This domain is very important and responsible for the whole current generation process, from absorption to charge transport. It is well documented that bimolecular recombination is the primary loss mechanism in most efficient OSC systems. It is assumed that due to the spatial dependence of carrier density distributions, phase separation, energetic disorder, and the re-release of free carriers that form a charge transfer state before recombining, this recombination can be significantly reduced compared to the Langevin description. It was also reported that energetic traps may play a significant role in shaping the kinetics of non-geminate recombination in OSC systems.^{34,43–45} However, as stated in Introduction, it is not clear how to decouple the effect of varying potential across the anode to get an accurate and quantitative description of these processes. Moreover, these mechanisms are hard to implement mathematically and are computation consuming, and therefore, the behavior of the OSC is at most being solved in one dimension, neglecting the distribution behavior of the contact resistance. Therefore, since we focused our attention on the interplay between the EOAL and the anode, few simplifications have been made in order to facilitate the calculation. We have used the simplest form of recombination associated with OSCs, i.e., Langevin driven bimolecular recombination. The implementation of different recombination mechanisms will be the topic of future work and is not reported here.

A commonly used model for describing charge transport within this disordered domain is found in the [supplementary material](#), and a detailed explanation can be found in the work by Koster *et al.*⁴⁶ Such simulations were performed in both the 1D and the 2D cases.^{47–49} We implemented our model for the two reported materials used in the simulations: poly[2-methoxy-5-(3', 7'-dimethyloctyloxy)-p-phenylene vinylene] (OC1C10-PPV) and [6,6]-phenyl C61-butyric acid methyl ester (PCBM) with 1:1 wt/wt ratio, but any combination of the donor-acceptor system can be used. The properties of these materials were used in this paper in order to verify the solution of the one dimensional case.

The back contact is an opaque and highly conductive metal with essentially zero resistivity. As such, the potential drop along the contact is assumed to be zero, which means that the value of the potential of the entire contact is determined by a constant applied voltage V_{app} and is position independent.

As mentioned in Introduction, the front contact has a finite conductivity due to its mandatory transparency. Therefore, this domain should be treated as a resistor with no charge accumulation, which is described by Laplace's equation

$$\Delta V_{an} = 0, \quad (1)$$

where V_{an} is the position dependent anode's potential.

In order to obtain a unique solution of the Laplace equation [Eq. (1)], it is necessary to specify the boundary conditions for the electrostatic potential. As a resistive medium, all free boundaries should satisfy Ohm's law. The left edge potential is determined by V_{app} . We next examine the top and right contact edges (see Fig. 1). As there is no current flow inside or outside, the electrostatic potential gradient parallel to these edges must be zero [Eq. (2)]

$$\frac{dV_{an}(x, t_{an})}{dz} = \frac{dV_{an}(L, z)}{dx} = 0. \quad (2)$$

As outlined in Introduction, since there is an extensive work on trying to achieve ohmic contacts,^{36–40} this investigation is also focused on such an ohmic case. Consequently, at the bottom edge, namely, the interface between the contact and the EOAL, Ohm's law takes the form described by Eq. (3) where the left side of the equation is the output current density from the EOAL (\vec{J}_{EOAL}) perpendicular to the interface calculated from the EOAL model

$$\vec{J}_{EOAL} = \sigma \vec{E}_{ITO}, \quad (3)$$

where σ is the material conductivity, which, in this case, is the commonly used Indium-Tin-Oxide (ITO). \vec{E}_{ITO} is the electric field at the bottom edge of the contact perpendicular to the interface. In opposition to the boundary conditions for the optical flux that are indeed position independent, the potential of the anode is position dependent, and it has to be determined self-consistently with the EOAL boundary. The interplay of both the contact and the EOAL is illustrated in Fig. 2.

As implied in the previous paragraph, the matching is done by using the results of one domain as a boundary condition for the other. The potential boundary for the EOAL

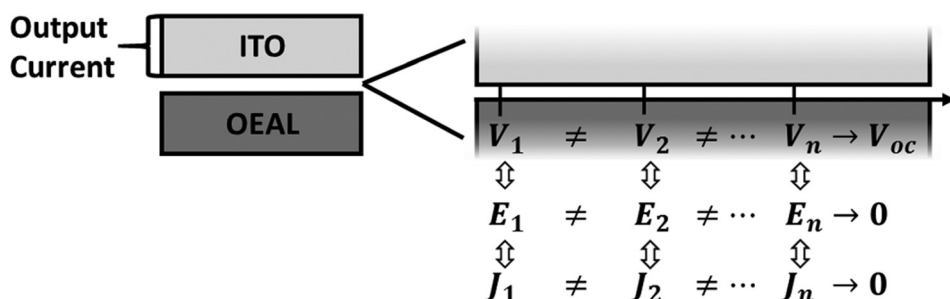


FIG. 2. The interface between the anode and EOAL. Voltage drop along the anode dictates a current reduction further away from contact and vice versa.

model at the contact's interfaces $\Delta V_{EOAL}(x)$ is determined by the difference between the blend band gap (E_{gap}) and the potential drop $V_{an}^{interface}(x)$ along the interface as shown in Eq. (4). Then, the current for the Laplace equation boundary condition [Eq. (3)] arises from the solution of the EOAL model. $V_{an}^{interface}(x)$ is a result of the Laplace equation

$$V_{EOAL}(x) = E_{gap} - V_{an}^{interface}(x). \quad (4)$$

The zero current flow inside or outside the left and right edges of the EOAL (see Fig. 1) is again dictating a zeroing of the electrostatic potential gradient parallel to these edges

$$\frac{dV_{EOAL}(0, z)}{dx} = \frac{dV_{EOAL}(L, z)}{dx} = 0. \quad (5)$$

It is essential also to specify the boundary conditions for the charge carrier densities. The Boltzmann statistics implies the following boundaries for ohmic contacts

$$n(x, 0) = N_c, \quad (6)$$

$$n(x, t_{EOAL}) = N_c \exp\left(-\frac{E_{gap}}{V_T}\right), \quad (7)$$

$$p(x, 0) = N_c \exp\left(-\frac{E_{gap}}{V_T}\right), \quad (8)$$

$$p(x, t_{EOAL}) = N_c. \quad (9)$$

The approach we used for the solution of our model was to iteratively solve the model describing the EOAL domain followed by the solution of the Laplace equation [Eq. (1)] within the anode and updating the relevant boundary condition after each iteration. This iterative process was done until convergence is achieved. In this manner, a matching between the anode and the EOAL interface was established. The implementation of the EOAL model together with its boundary conditions was carried out according to the Scharfetter-Gummel discretization scheme.⁵⁰ All the calculations were performed using Matlab, and the linear equations were solved by the built-in function of the Bi-conjugate gradient stabilized method.⁵¹ Likewise, the solution of the Laplace equation [Eq. (1)] was done using the finite-difference approach.

This approach was found to be highly stable and accurate; however, from the computational point-of-view, we have a serious drawback due to a huge difference between the device thickness and its length. While the device thickness is around 100 nm, the length of a standard device varies from one millimeter to a few centimeters. Therefore, the number of mesh-points in the longitudinal direction should be significantly high to get a sufficient accuracy, which results in an extensive amount of computation time. For optimized performance, we chose the longitudinal and vertical spacing between two neighbor mesh-points to be $h = 1 \mu\text{m}$ and $k = 2 \text{ nm}$, respectively. We did not see any significant improvement in the accuracy of the calculation with finer meshes. However, even this mesh that has three orders of magnitude difference between the two axes results in an extensive amount of time for each iteration. To overcome this drawback, we implemented a method that reduces the

amount of executions of the EOAL model by pre-estimating the initial guess of the iterative process mentioned above. The full description of this method is depicted in the [supplementary material](#).

III. RESULTS

We used the model described above to investigate the effects of the OSC length on its characteristics. We solved the device's equations as a function of the device's length for various anode conductivities and for lengths ranging from 1 mm to 2.5 cm under one sun condition. From the solutions of the simulation, we extracted the device IV characteristics and the additional relevant electrical properties that demonstrate the effect of the device's length. Figure 3 shows the device output current at short circuit conditions (I_{sc}) as a function of the device's length for three different anode conductivities.

At small device lengths (smaller than 0.5 cm), the three curves are coinciding, meaning that the low anode conductivity values as a negligible influence on the short circuit current. At low device length regions (smaller than around 0.7, 1, and 1.5 cm for conductivities of 100, 200, and 500 S/cm, respectively), I_{sc} increases linearly. However, as the device length is further increased, I_{sc} saturates and the curves become more and more divergent, a behavior which is indicative of a length independency and strong anode's conductivity impact on the cell performance.

This effect is due to the finite conductivity of the anode, which dictates a voltage drop along the EOAL/anode interface. This drop means that as the distance from the device output increases, the relevant part of the device works at close to open circuit conditions instead of short circuit. This behavior is demonstrated for $\sigma = 100 \text{ S/cm}$ for different device lengths in Fig. 4.

It is clear from Fig. 4 that as the length of the device increases, a larger voltage drop is developed along the EOAL/anode interface. This means that, for example, at a length of 1 cm, the right edge of the device is very close to

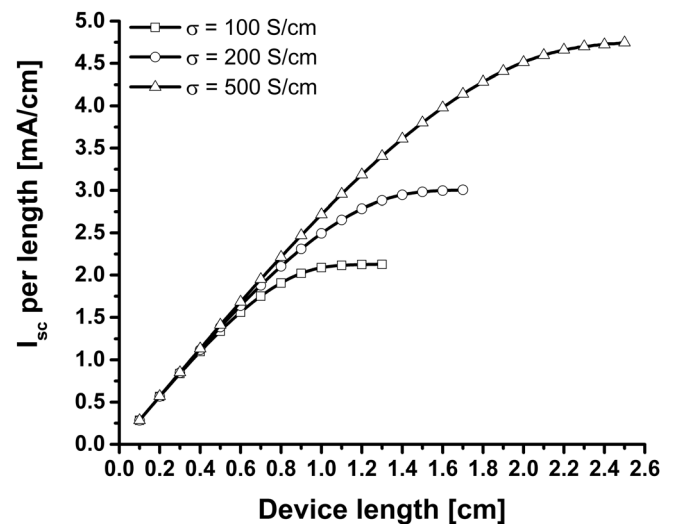


FIG. 3. The short circuit current at the device output as a function of the device length at three different anode conductivities—(square) $\sigma = 100 \text{ S/cm}$, (circle) $\sigma = 200 \text{ S/cm}$, (triangle) $\sigma = 500 \text{ S/cm}$.

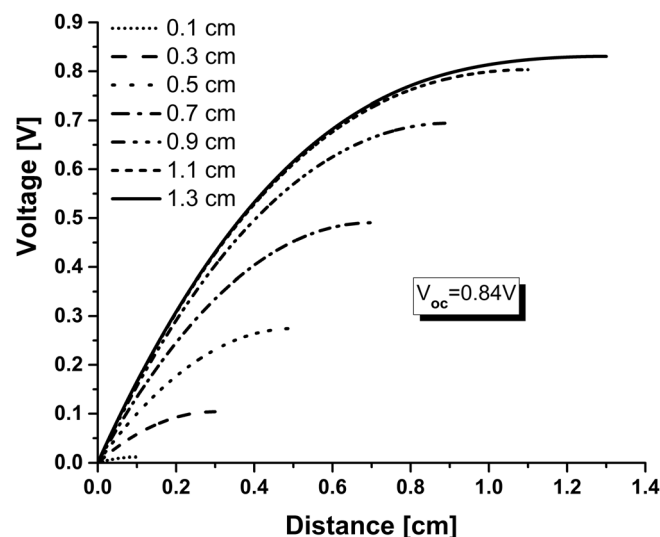


FIG. 4. Voltage drop along the EOAL/Anode interface under short circuit conditions for various device lengths. The left side is fixed to a zero bias, and as the distance from the contact grows, the voltage builds up and approaches open circuit conditions $V_{oc} = 0.84$ V.

open circuit conditions ($V_{oc} = 0.84$ V) and therefore does not contribute to the current. The voltage drop along the EOAL/Anode interface for the other anode conductivities under investigation exhibits similar behavior and are presented in the [supplementary material](#).

On the other hand, to demonstrate the impact of the anode's conductivity, we present the voltage on the right side of each of the three different devices as a function of length for each conductivity value, (Fig. 5), i.e., the voltage drop along the interface. It can be seen that as the conductivity increases, the device length can be extended without experiencing a near open circuit condition further from the anode's output.

The short circuit current is an important quantity for the characterization of a solar cell. However, since the output power at this point is zero, it is important to study the entire

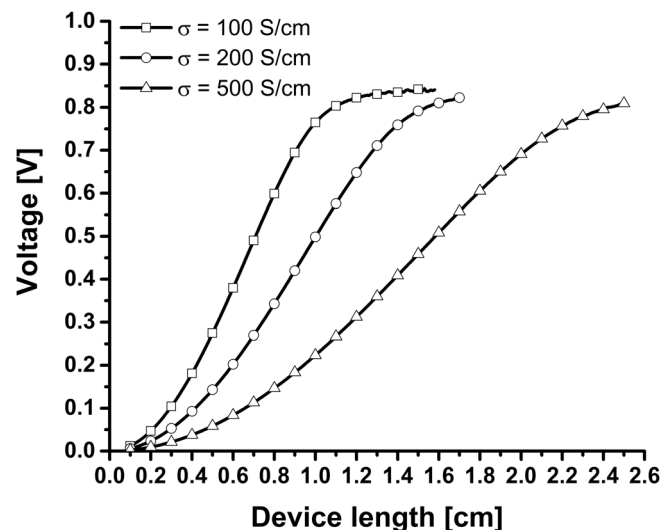


FIG. 5. Voltage at the interface at the right side of the device (far from anode output—see Fig. 1), i.e., the voltage drop along the interface at different anode's conductivities—(square) $\sigma = 100$ S/cm, (circle) $\sigma = 200$ S/cm, and (triangle) $\sigma = 500$ S/cm.

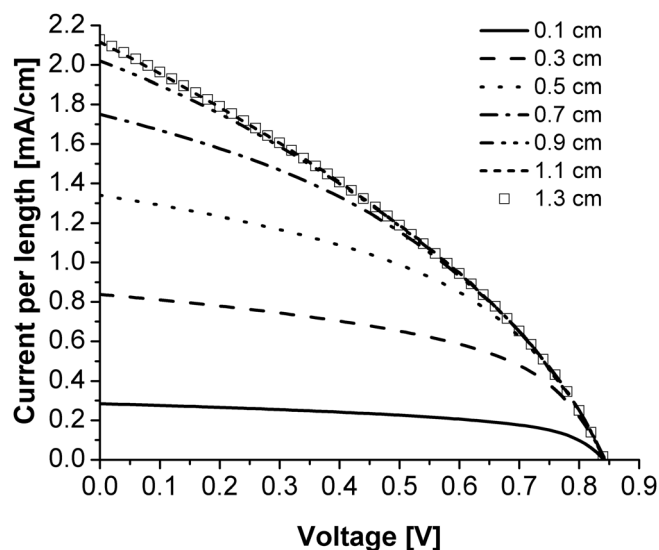


FIG. 6. IV curves for different device lengths. The IV curve for the device length of 1.3 cm represented as squares for clarity.

IV curve and in particular, the behavior of the maximum power point. The dependence of the entire device IV curve of different device lengths for $\sigma = 100$ S/cm is shown in Fig. 6 (the IV curves for $\sigma = 200$, and 500 S/cm are presented in the [supplementary material](#)).

Figure 6 demonstrates that almost all of the key parameters of the OSC, namely, I_{sc} , P_m , FF deteriorated as the length of the device increases. The saturation referred to above (at Fig. 4) of I_{sc} can be seen here from a more general point of view. That is, I_{sc} is not as twice as large for a doubled length of the device although the amount of sun light is twice as much. There is a reduction in the Fill-Factor (FF) as the cell length increases. This can be qualitatively observed from the shape of the curve. The IV curve at 1 mm has a quadratic shape, but as the length increases, the curve tends to be more of a straight line. In Fig. 7, the calculated FF for different anode's conductivities is presented to show this quantitative behavior.

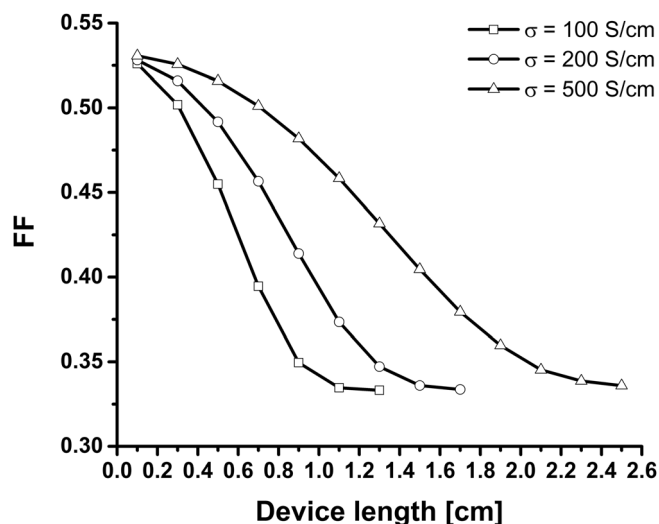


FIG. 7. The Fill Factor as a function of device's length at different anode's conductivities—(square) $\sigma = 100$ S/cm, (circle) $\sigma = 200$ S/cm, and (triangle) $\sigma = 500$ S/cm.

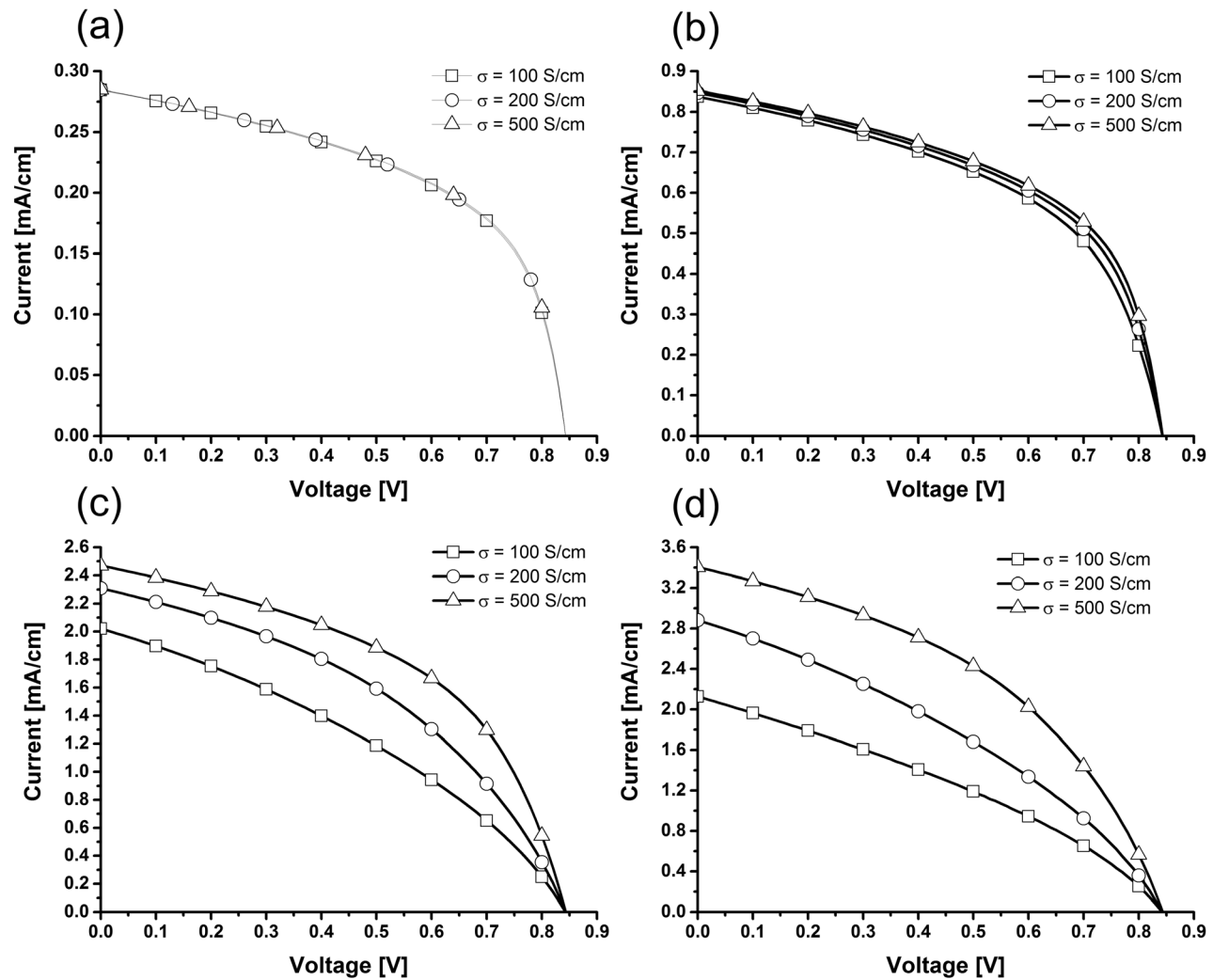


FIG. 8. IV curves at fixed lengths, (a) 0.1 cm, (b) 0.3 cm, (c) 0.9 cm, and (d) 1.3 cm, for different anode's conductivities— (square) $\sigma = 100$ S/cm, (circle) $\sigma = 200$ S/cm, and (triangle) $\sigma = 500$ S/cm.

To further examine the effect of anode's conductivity, we fixed the length of the solar cell and calculated the IV curves for different conductivities (Fig. 8).

The IV curves in Fig. 8(a) are overlapping each other. It is an indication of the insignificance of the conductivity of the anode at very small device lengths. Nevertheless, already at 0.3 cm (Fig. 8(b)), a separation between different conductivities is observed. At higher device lengths (Figs. 8(c) and 8(d)), high values of conductivities are becoming crucial for achieving best solar cell performance (other IV curves for different lengths are presented in the [supplementary material](#)).

The behavior of I_{sc} and FF obviously affects the most important parameter from the point of view of the industry, the maximum power (P_m) of the device. The dependence of the maximum power point on the device length and for different anode conductivities is represented in Fig. 9. We can see that P_m tends to saturate very fast (even before the saturation of both the short circuit current and the FF). It means that a further increase in the device length above a certain length just reduces the overall efficiency as we extract the same power from larger devices.

The lengths at which the maximum power saturated for different conductivities are shown in Table I.

IV. CONCLUSION

OSCs could play an important role in areas unsuitable for their corresponding inorganic counterparts. Nevertheless,

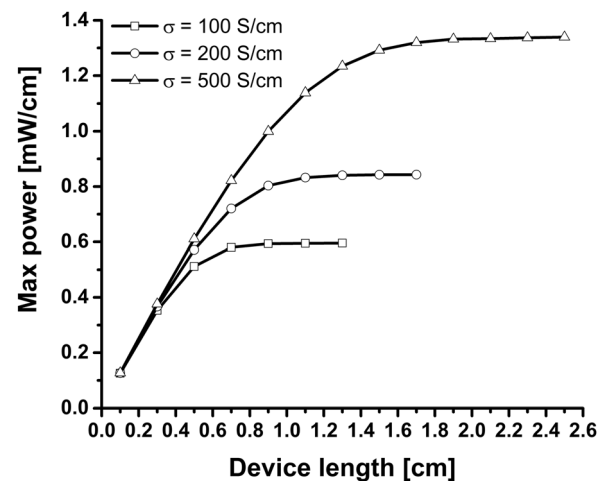


FIG. 9. The Maximum power point as a function of device's length for different anode's conductivities—(square) $\sigma = 100$ S/cm, (circle) $\sigma = 200$ S/cm, and (triangle) $\sigma = 500$ S/cm.

TABLE I. The length in which the maximum power of the device starts to saturate for different anode conductivities.

Conductivity σ (S/cm)	Saturation length (cm)
100	0.8
200	1.2
500	2.1

the issue of scaling up OSCs prevents them from being practical. As stated in the Introduction, experimental observations show drastic deterioration in all the key parameters as the OSC size increases. In order to explain and understand the observations as well as predict the large area device's behavior, we successfully developed an innovative 2D simulation based on the fundamental physics of charge transport in organic materials and ITO.

The simulation that includes the entire device's domains reveals a significant loss in power as the length of the device increases. This power loss is highly sensitive to the conductivity of the anode and saturates very fast for lower values of anode's conductivities. We showed that both I_{sc} and FF are experiencing an undesirable behavior at high lengths, which is consistent with results arising from the basic conventional equivalent circuit model.⁵² This in return damages the device output power and its performance. This is a direct outcome of the anode resistivity. Previous works suggested that the device power loss, which is primarily due to the anode, acts as if it was a regular resistor, namely, $P_{ITO} = R_{sheetITO} \times A \times J^2$. Here, we argue that the power loss is indeed a product of the voltage drop along the anode but is not linear with respect to the size. The voltage drop results in a reduction in the generated current in regions further away from the contact. This loss process deviates from the loss mechanism in a standard resistor as it dictates a reduction in the light-to-current conversion in the farther parts of the device. As a result, the device undergoes rapid output power saturation. These results are consistent with observation of reported experiments.^{7–10,29} Our results point out for significant lengths (around 0.8, 1.2, and 2.1 cm for $\sigma = 100$, 200 and 500 S/cm) where the power saturates. They can also be used to identify the lengths where the actual deviation from linear increase in the short circuit current and maximum power point is observed (around 0.4, 0.5, and 0.7 cm for $\sigma = 100$, 200, and 500 S/cm). These two points give us the necessary information for the future design of OSC anodes, and it paves the way towards optimizing the performance of OSCs combined with metal grids on the top.

SUPPLEMENTARY MATERIAL

See [supplementary material](#) for the electric model description, the iterative method, and additional IV graphs.

ACKNOWLEDGMENTS

This research was supported by the Israel Science Foundation as part of the ISF-NSFC joint program 2192/15.

¹M. A. Green, K. Emery, Y. Hishikawa, W. Warta, and E. D. Dunlop, *Prog. Photovoltaics: Res. Appl.* **24**(7), 905–913 (2016).

- ²C. D. Müller, A. Falcou, N. Reckefuss, M. Rojahn, V. Wiederhirn, P. Rudati, H. Frohne, O. Nuyken, H. Becker, and K. Meerholz, *Nature* **421**(6925), 829–833 (2003).
- ³S. R. Forrest, *Nature* **428**(6986), 911–918 (2004).
- ⁴C. G. Granqvist, *Thin Solid Films* **564**, 1–38 (2014).
- ⁵M. Kamalifarvestani, R. Saidur, S. Mekhilef, and F. Javadi, *Renewable Sustainable Energy Rev.* **26**, 353–364 (2013).
- ⁶D. Angmo, I. Gonzalez-Valls, S. Veenstra, W. Verhees, S. Sapkota, S. Schiefer, B. Zimmermann, Y. Galagan, J. Sweelssen, and M. Lira-Cantu, *J. Appl. Polym. Sci.* **130**(2), 944–954 (2013).
- ⁷J. Yeo, J. Yun, S. Kim, D. Kim, J. Kim, and S. Na, *Semicond. Sci. Technol.* **26**(3), 34010 (2011).
- ⁸D. Gao and D. S. Seferos, *Sol. Energy Mater. Sol. Cells* **95**(12), 3516–3519 (2011).
- ⁹M. Al-Ibrahim, H. K. Roth, and S. Sensfuss, *Appl. Phys. Lett.* **85**, 1481–1483 (2004).
- ¹⁰D. Gupta, M. Bag, and K. Narayan, *Appl. Phys. Lett.* **93**(16), 163301 (2008).
- ¹¹Y. Galagan, I. G. de Vries, A. P. Langen, R. Andriessen, W. J. Verhees, S. C. Veenstra, and J. M. Kroon, *Chem. Eng. Process.* **50**(5), 454–461 (2011).
- ¹²A. Pandey, J. Nunzi, B. Ratier, and A. Moliton, *Phys. Lett. A* **372**(8), 1333–1336 (2008).
- ¹³J. Halls, K. Pichler, R. Friend, S. Moratti, and A. Holmes, *Appl. Phys. Lett.* **68**(22), 3120 (1996).
- ¹⁴M. Stoessel, G. Wittmann, J. Staudigel, F. Steuber, J. Blässing, W. Roth, H. Klausmann, W. Rogler, J. Simmerer, and A. Winnacker, *J. Appl. Phys.* **87**(9), 4467–4475 (2000).
- ¹⁵K. Ellmer, *Nat. Photonics* **6**(12), 809–817 (2012).
- ¹⁶S. De and J. N. Coleman, *ACS Nano* **4**(2713), 2713–2720 (2010).
- ¹⁷S. Choi, W. J. Potscavage, Jr., and B. Kippelen, *J. Appl. Phys.* **106**(5), 54507 (2009).
- ¹⁸Y. Galagan, B. Zimmermann, E. W. Coenen, M. Jørgensen, D. M. Tanenbaum, F. C. Krebs, H. Gorter, S. Sabik, L. H. Slooff, and S. C. Veenstra, *Adv. Energy Mater.* **2**(1), 103–110 (2012).
- ¹⁹S. Na, S. Kim, J. Jo, and D. Kim, *Adv. Mater.* **20**(21), 4061–4067 (2008).
- ²⁰F. Zhang, M. Johansson, M. R. Andersson, J. C. Hummelen, and O. Inganäs, *Adv. Mater.* **14**(9), 662–665 (2002).
- ²¹L. Gomez De Arco, Y. Zhang, C. W. Schlenker, K. Ryu, M. E. Thompson, and C. Zhou, *ACS Nano* **4**, 2865–2873 (2010).
- ²²Y. H. Kim, C. Sachse, M. L. Machala, C. May, L. Müller-Meskamp, and K. Leo, *Adv. Funct. Mater.* **21**(6), 1076–1081 (2011).
- ²³K. Tvingstedt and O. Inganäs, *Adv. Mater.* **19**(19), 2893–2897 (2007).
- ²⁴M. Kang, M. Kim, J. Kim, and L. J. Guo, *Adv. Mater.* **20**(23), 4408–4413 (2008).
- ²⁵S. Park, W. Jeong, D. Kim, J. Kim, D. C. Lim, J. H. Kim, J. Kim, and J. Kang, *Appl. Phys. Lett.* **96**(17), 84 (2010).
- ²⁶J. Yu, G. H. Jung, J. Jo, J. S. Kim, J. W. Kim, S. Kwak, J. Lee, I. Kim, and D. Kim, *Sol. Energy Mater. Sol. Cells* **109**, 142–147 (2013).
- ²⁷J. E. Carlé, T. R. Andersen, M. Helgesen, E. Bundgaard, M. Jørgensen, and F. C. Krebs, *Sol. Energy Mater. Sol. Cells* **108**, 126–128 (2013).
- ²⁸M. Hösel, R. R. Søndergaard, M. Jørgensen, and F. C. Krebs, *Energy Technol.* **1**(1), 102–107 (2013).
- ²⁹A. Manor, E. A. Katz, T. Tromholt, B. Hirsch, and F. C. Krebs, *J. Appl. Phys.* **109**(7), 074508 (2011).
- ³⁰Y. Galagan, E. W. Coenen, S. Sabik, H. H. Gorter, M. Barink, S. C. Veenstra, J. M. Kroon, R. Andriessen, and P. W. Blom, *Sol. Energy Mater. Sol. Cells* **104**, 32–38 (2012).
- ³¹Y. Galagan, E. W. Coenen, B. Zimmermann, L. H. Slooff, W. J. Verhees, S. C. Veenstra, J. M. Kroon, M. Jørgensen, F. C. Krebs, and R. Andriessen, *Adv. Energy Mater.* **4**(2), 1300498 (2014).
- ³²M. Denhoff and N. Drolet, *Sol. Energy Mater. Sol. Cells* **93**(9), 1499–1506 (2009).
- ³³L. Tzabari, V. Zayats, and N. Tessler, *J. Appl. Phys.* **114**(15), 154514 (2013).
- ³⁴L. Tzabari, J. Wang, Y. Lee, J. W. Hsu, and N. Tessler, *J. Phys. Chem. C* **120**(19), 10146–10155 (2016).
- ³⁵N. Tessler, *J. Appl. Phys.* **118**(21), 215501 (2015).
- ³⁶Z. Tan, Y. Vaynzof, D. Credgington, C. Li, M. T. Casford, A. Sepe, S. Huettnier, M. Nikolka, F. Paulus, and L. Yang, *Adv. Funct. Mater.* **24**(20), 3051–3058 (2014).
- ³⁷C. J. Brabec, S. E. Shaheen, C. Winder, N. S. Sariciftci, and P. Denk, *Appl. Phys. Lett.* **80**(7), 1288–1290 (2002).
- ³⁸D. Chirvase, Z. Chiguvare, M. Knipper, J. Parisi, V. Dyakonov, and J. Hummelen, *J. Appl. Phys.* **93**(6), 3376–3383 (2003).
- ³⁹G. Li, C. Chu, V. Shrotriya, J. Huang, and Y. Yang, *Appl. Phys. Lett.* **88**(25), 253503 (2006).

- ⁴⁰D. Zhao, P. Liu, X. Sun, S. Tan, L. Ke, and A. Kyaw, *Appl. Phys. Lett.* **95**(15), 275 (2009).
- ⁴¹D. Gupta, S. Mukhopadhyay, and K. Narayan, *Sol. Energy Mater. Sol. Cells* **94**(8), 1309–1313 (2010).
- ⁴²A. Manor, E. A. Katz, R. Andriessen, and Y. Galagan, *Appl. Phys. Lett.* **99**(17), 235 (2011).
- ⁴³C. M. Proctor, M. Kuik, and T. Nguyen, *Prog. Polym. Sci.* **38**(12), 1941–1960 (2013).
- ⁴⁴A. J. Ferguson, N. Kopidakis, S. E. Shaheen, and G. Rumbles, *J. Phys. Chem. C* **115**(46), 23134–23148 (2011).
- ⁴⁵D. Veldman, O. Ipek, S. C. Meskers, J. Sweelssen, M. M. Koetse, S. C. Veenstra, J. M. Kroon, S. S. V. Bavel, J. Loos, and R. A. Janssen, *J. Am. Chem. Soc.* **130**(24), 7721–7735 (2008).
- ⁴⁶L. Koster, E. Smits, V. Mihailetschi, and P. Blom, *Phys. Rev. B* **72**(8), 85205 (2005).
- ⁴⁷G. A. Buxton and N. Clarke, *Modell. Simul. Mater. Sci. Eng.* **15**(2), 13 (2006).
- ⁴⁸W. S. Koh, M. Pant, Y. A. Akimov, W. P. Goh, and Y. Li, *IEEE J. Photovoltaics* **1**(1), 84–92 (2011).
- ⁴⁹R. Häusermann, E. Knapp, M. Moos, N. Reinke, T. Flatz, and B. Ruhstaller, *J. Appl. Phys.* **106**(10), 104507 (2009).
- ⁵⁰S. Selberherr, *Analysis and Simulation of Semiconductor Devices* (Springer Science & Business Media, 2012).
- ⁵¹A. H. Van der Vorst, *SIAM J. Sci. Stat. Comput.* **13**(2), 631–644 (1992).
- ⁵²J. D. Servaites, S. Yeganeh, T. J. Marks, and M. A. Ratner, *Adv. Funct. Mater.* **20**(1), 97–104 (2010).